Chinar R. Aphale
Department of Mechanical Engineering,
University of Michigan,
Ann Arbor, MI 48105
e-mail: caphale@umich.edu

Jinhyun Cho
Department of Mechanical Engineering,
University of Michigan,
Ann Arbor, MI 48105
e-mail: jinhyunc@umich.edu

William W. Schultz
Department of Mechanical Engineering,
University of Michigan,
Ann Arbor, MI 48105
e-mail: schultz@umich.edu

Steven L. Ceccio
Department of Mechanical Engineering,
University of Michigan,
Ann Arbor, MI 48105
e-mail: ceccio@umich.edu

Takao Yoshioka
Dynax Corporation,
Hokkaido, Japan
e-mail: yoshioka-t@mail.dxj.co.jp

Henry Hiraki
Dynax Corporation,
Hokkaido, Japan
e-mail: hiraki-h@mail.dxj.co.jp

Modeling and Parametric Study of Torque in Open Clutch Plates

The relative motion of the friction and separator plates in wet clutches during the disengaged mode causes viscous shear stresses in the fluid passing through the 100 microns *gap. This results in a drag torque on both the disks that wastes energy and decreases fuel economy. The objective of the study is to develop an accurate mathematical model for the above problem with verification using* FLUENT *and experiments. Initially we two consider flat disks. The mathematical model calculates the drag torque on the disks and the 2D axisymmetric solver verifies the solution. The surface pressure distribution on the plates is also verified. Then, 3D models of one grooved and one flat disk are tested using CFD, experiments and an approximate 3D mathematical model. The number of grooves, depth of groove and clearance between the disks are studied to understand their effect on the torque. The study determines the pressure field that eventually affects aeration incipience (not studied here). The results of the model, computations and experiments corroborate well in the single-phase regime.* [DOI: 10.1115/1.2162553]

1 Introduction

The fluid motion over a single rotating plate has been studied extensively. Von Karman [1] studied the problem of an infinite disk rotating in quiescent fluid revealing the swirling flow patterns over the disk. He reduced the equations of motion to a nonlinear differential equation using the assumption of axisymmetry and similarity. His work and the subsequent solution to those equations by Cochran [2] determined the nature of flow field over the rotating disk. Fluid entrains axially and exits the disk surface radially. This problem has many similarities to rotating turbo machinery such as compressors and centrifugal pumps. Here, our primary interest is in the open clutch system where two disks rotate at different speeds. Some early work with two co-rotating disks is attributed to Batchelor [3] and Stewartson [4]. Batchelor proposed that the core of fluid between the two plates away from the boundary layer on the disks rotates with constant angular velocity while Stewartson suggested that boundary layer forms only on the rotating disk and that the remaining fluid will not rotate if one disk is stationary or counter-rotating.

Further, we study the case where the plate separation is small and lubrication scaling is appropriate. Recent work by Kitamura [5] highlights this asymptotic treatment of the Navier-Stokes equations. Since the gap between the two disks is very small compared to their radii, the equations can be scaled accordingly. The relative effects of inertial, gravitational and surface tension forces were assessed. These simplified equations are the basis of the mathematical model for the problem in this paper. The ease of pressure and shear stress distribution calculations using the model makes this tool very useful.

This study focuses on reducing shear stress and hence consequently the drag on the disks. In an open clutch system, a rotating friction plate (FP) and a stationary separator plate (SP) are 100 microns apart. An oil film is maintained between the disks for lubrication when the clutch disks are brought together for engagement. However in the disengaged mode, the viscous shearing of this oil film causes unnecessary torque on both disks. This wastes energy that decreases fuel economy.

Schade [6], Fish [7], and Lloyd [8] empirically determine trends regarding geometric parameters such as groove patterns, depths as well as clearance and flow rate. They also indicate the importance of disk waviness in reducing drag torque. This study is restricted to flat (not wavy) plates, with the exception of possible grooves [9–11].

The most important aspect that reduces the torque is aeration. Air infiltration between the two disks reduces torque substantially since air has low viscosity. The analysis here will show where aeration is likely to occur. The flow rate is very important in determining the pressure distribution along the disks however its direct effect on drag torque for nonaerated lubrication is minimal. As a result, varying flow rates are not considered in these single-phase simulations. We leave aeration study to subsequent publication.

Yuan [12] also compares computations of grooved plates with experiments. Their results suggest that surface tension has an im-

Contributed by the Tribology Division of ASME for publication in the JOURNAL OF TRIBOLOGY. Manuscript received February 25, 2004; final manuscript received September 19, 2005. Review conducted by Lyndon S. Stephens .

 Copyright © 2006 by ASME

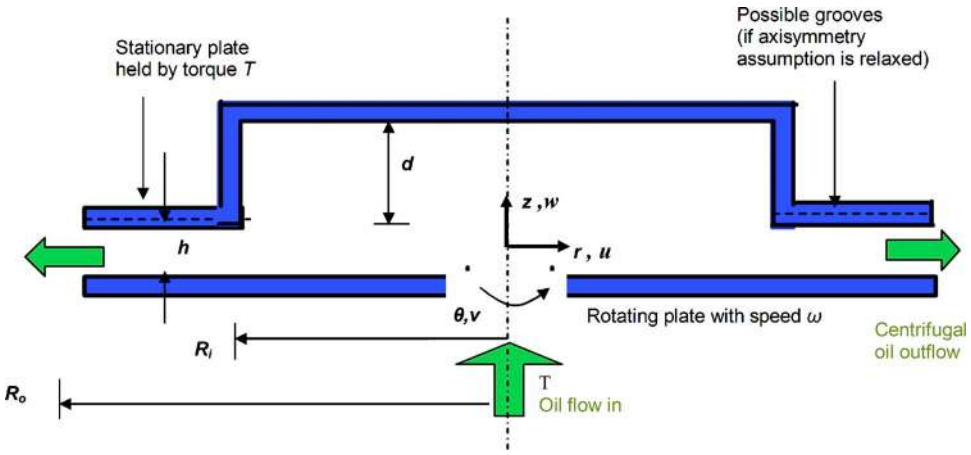

Fig. 1 Schematic diagram of the apparatus, showing oil entering axially from the center of rotating plate and exiting radially at $r=R_o$ due to centrifugal action. The origin of the coordinate system is on the symmetry axis halfway between the two plates. The relevant dimensions are shown.

portant role in the incipience of aeration. The parametric study of Kitabayashi [13] concluded that speed is the most important parameter that affects drag torque.

In Sec. 2, we start with the asymptotic analysis of the Navier-Stokes equations and the subsequent derivation of the lubrication model. Section 3 describes the 2D axisymmetric modeling of the flow using FLUENT. Section 4 explains the experimental apparatus. Section 5 comprises of 3D computations and contours of important solution variables at low rotation speed. Section 6 compares the model, computations and experiments. Both the pressure distribution and shear stress distribution are considered for an effective comparison even though we are primarily interested in the shear stress values. Section 7 enlists the conclusions of the study.

2 Mathematical Model

Asymptotic Analysis of Navier-Stokes Equations. In this section, the momentum equations are reduced by making lubrication approximations with reduced equations offering us an exact local velocity profile (Fig. 1). The flow is assumed to be steady and axisymmetric. Hence, $\partial/\partial t=\partial/\partial\theta=0$. In addition, r, R_i, and R_o are scaled by R_m, z is scaled by h, v is scaled by ωR_m, u is scaled by $\omega^2 R_m h^2\rho/\mu$, p is scaled by ρv_s^2, w is scaled by $\omega^2 h^3\rho/\mu$, Q is scaled by $u_s R_m$ and τ is scaled by $\rho\omega^2 h^2$. The usual lubrication approximations are made; $h \ll R_m$; $w_s \ll u_s$ and the inertial forces in the axial and tangential directions vanish such that $\mathrm{Re}_w = w_s h\rho/\mu \to 0$ and $\mathrm{Re}_u = u_s h\rho/\mu \to 0$. The clearance between the two plates, h, is constant. Also, we define the parameter $\varepsilon = h/R_m$.

Even though this is a lubrication problem, the scale chosen for pressure is not the viscous type but an inertial one. This is nonstandard but can be justified since centrifugal force is the dominant effect driving the fluid in the radial direction.

Putting the scaled variables in r direction momentum equation and noting that $\omega^2 R_m h^2\rho/\mu = u_s$, the lowest-order r momentum equation in ε is

$$\frac{\partial p}{\partial r} - \frac{v^2}{r} = \frac{\partial^2 u}{\partial z^2}. \tag{1}$$

Similarly, the z momentum equation is

$$\frac{\partial p}{\partial z} = 0, \tag{2}$$

and the θ momentum equation becomes

$$\frac{\partial^2 v}{\partial z^2} = 0. \tag{3}$$

The continuity equation becomes,

$$\frac{1}{r}\frac{\partial (ru)}{\partial r} + \frac{\partial w}{\partial z} = 0. \tag{4}$$

The boundary conditions on the disk are $u(z=\pm h/2)=w(z=\pm h/2)=v(z=-h/2)=v(z=h/2)-\omega r=0$. At the inlet and outlet two more conditions are needed; one on pressure and the other on radial component of velocity (flow rate). However, we can choose to specify conditions on the inlet and outlet pressures and leave the flow rate unspecified

$$p(r=R_i) - p_o = p(r=R_o) - p_o = 0.$$

Equations (1)–(4) govern the problem. The pressure is just a function of radius r and is independent of z. Also, the tangential velocity profile is linear with no slip conditions at the walls. On specifying the appropriate boundary conditions, the above set of partial differential equations constitute a well-posed problem with four equations and an equal number of unknowns.

Solution of (3) gives us the exact profile for the tangential component of velocity v.

$$v = r\left(z + \frac{1}{2}\right).$$

Using this and noting that the pressure gradient is independent of z from (2), we integrate (1) and upon applying boundary conditions obtain

$$u = \frac{dp}{dr}\left(\frac{z^2}{2} - \frac{1}{8}\right) - \frac{z^2 r}{2}\left(\frac{z^2}{6} + \frac{z}{3} + \frac{1}{4}\right) + \frac{4zr}{96} + \frac{7r}{192}.$$

This profile for the radial velocity u is an exact solution of the lubrication equations. Finally, the pressure gradient is calculated using continuity.

$$\int_{-1/2}^{1/2} u(z)dz = \frac{Q}{2\pi r},$$

and hence

$$\frac{dp}{dr} = \frac{12\mu}{h^2}\left(\frac{r}{40} - \frac{Q}{2\pi r}\right).$$

The pressure profile is obtained by integrating the above equation and using the boundary condition that the pressure at outer edge is ambient

$$P - P_o = 12\left[\frac{1}{80}(r^2 - R_o^2) - \frac{Q}{2\pi}\ln\frac{r}{R_o}\right].$$

Approximate Solution of the Equations. The inertial term is normally absent in lubrication theory and the velocity profile is parabolic. However here, the inertial term is not only dominant but also has a z dependence. For an approximate model, the inertial term is modeled by some term which is independent of z. More simplifications allow these equations to become ordinary differential equations. The first requires w to be neglected. This assumption is aided by the constant geometry in the radial direction. The clearance remains constant and as a result the fluid is not accelerated or decelerated as it passes between the two plates. This assumption is checked in the *a posteriori* computations to follow. Thus, continuity reduces to the trivial form

$$u(r,z) = \frac{f(z)}{r}.$$

This assumption is also required for the above exact model. The second assumption is that $f(z)$ is a second-order polynomial in z. This means that the diffusion term in (1) is independent of z. Equation (2) suggests that pressure is independent of z. But, the centrifugal force term in (1) is strongly a function of z. Thus the two assumptions not only introduce a contradiction in the governing equation, but also have changed the nature of the system to four equations and three unknowns.

Assuming a second-order polynomial profile in $z(\partial^3 u/\partial z^3 = 0)$ that satisfies the boundary conditions and continuity, the radial velocity is given by $u \propto (1/4 - z^2)/r$. Now the second term on the left hand side (LHS) of (1) is z-dependent. Therefore, we must assume an averaged centrifugal force from the mean of the tangential velocity between top and bottom plates. Therefore, the dimensionless average velocity is $\nu = 0.5r$. The factor of 0.5 was later modified to 0.565 to better compare to computational results.

Letting $\langle u \rangle$ denote the average radial velocity at any radius r,

$$\langle u \rangle = \frac{Q}{2\pi r},$$

where Q is the volumetric flow rate and the definition of average is

$$\langle u \rangle = \int_{-1/2}^{1/2} u(z)dz.$$

Upon applying the quadratic radial velocity assumption and recognizing that Q is constant gives

$$u(z,r) = \frac{3Q}{\pi r}\left(\frac{1}{4} - z^2\right).$$

To check the validity of the approximations, the terms dropped from the original Navier-Stokes r direction momentum are compared with the most dominant term. The L_2 norm is used to compare the terms. If $g(x)$ is a function of x defined in the domain $a \leqslant x \leqslant b$, then the L_2 norm of $g(x)$ is defined by

$$\|g(x)\|_2 = \sqrt{\int_a^b (g(x))^2 dx}$$

Assuming typical dimension values for these constants

$$Q = .00634; R_o = 1.05$$

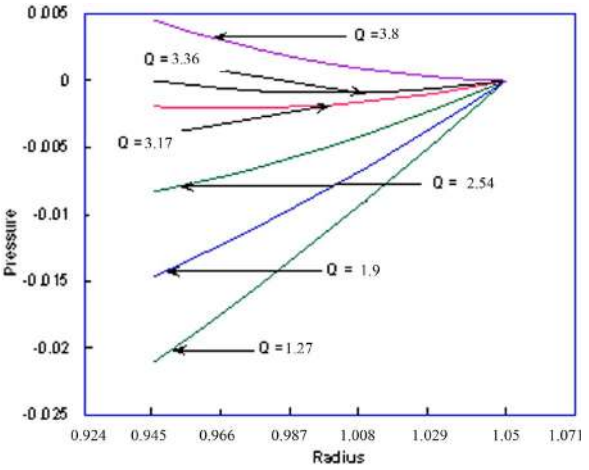

Fig. 2 Pressure distribution vs radial coordinate. The case where pressures at both the inner and outer radii are zero corresponds to the natural flow rate of the system. Pressure is normalized with ρv_s^2 and radius with R_m.

$$R_i = 0.95;$$

The compared terms are

$$\frac{\|uu_r\|_2}{\|u_{zz}\|_2} = 1.7 \times 10^{-7}; \frac{\|u/r^2\|_2}{\|u_{zz}\|_2} = 7 \times 10^{-11}; \frac{\|(ru_r)_r/r\|_2}{\|u_{zz}\|_2} = 5 \times 10^{-11}$$

The above procedure checks the asymptotic result obtained previously. The sample values were chosen to be in accord with the assumptions made while choosing the scales. Thus, the centrifugal force and the viscous diffusion term are the most dominant terms in the r-momentum equation along with the pressure gradient.

$$\frac{dp}{dr} - \frac{\nu^2}{r} = \frac{\partial^2 u}{\partial z^2}.$$

The assumed radial and tangential velocity profiles are used to solve the above equation for pressure p

$$\nu = \frac{1}{2}r \text{ and } u(z,r) = \frac{3Q}{\pi r}\left(\frac{1}{4} - z^2\right)$$

Solving this ordinary differential equation (ODE) in r, and imposing the boundary condition $p(r=R_o)=p_o$ gives

$$p - p_o = \frac{6Q}{\pi}\ln\left(\frac{R_o}{r}\right) + \frac{1}{8}(r^2 - R_o^2). \quad (5)$$

Thus, the pressure obtained at each point in the flow is a function of r. Figure 2 shows how the pressure distribution varies with varying flow rate. The condition where the gauge pressure at inlet and exit is zero corresponds to the natural flow rate of the device. To promote aeration in the plates, the flow rate supplied should be less than what the plates can pump out due to centrifugal action. Only in such a case will air be entrained from the outer radius and torque on the plates reduced. This natural flow system rate can be calculated using (5) for a particular flow, speed and plate clearance.

Torque Calculations. To find the torque, the stresses acting on the plates are calculated. After considering the axisymmetric assumption, the components of shear stress in cylindrical coordinates reduce to

$$\tau_{zz} = 2\frac{\partial w}{\partial z}; \quad \tau_{zr} = \left(\frac{1/\varepsilon \partial u}{\partial z} + \varepsilon \frac{\partial w}{\partial r}\right); \quad \tau_{\theta z} = \tau_{z\theta} = \left(\frac{\varepsilon}{r}\frac{\partial w}{\partial \theta} + \nu_s / w_s \frac{\partial \nu}{\partial z}\right).$$

In the model, since w is much smaller than both u and ν, the axisymmetric equations reduce to

$$\tau_{zz} = 0; \quad \tau_{zr} = \left(\frac{\partial u}{\partial z}\right) 1/\varepsilon; \quad \tau_{\theta z} = \tau_{z\theta} = \left(\frac{\partial \nu}{\partial z}\right) \nu_s / w_s.$$

The velocity profiles are

$$u(z,r) = \frac{3Q\left(\frac{1}{4} - z^2\right)}{\pi r}; \quad \nu = r\left(z + \frac{1}{2}\right).$$

Thus,

$$\tau_{zr} = \frac{-6Qz}{\pi r \varepsilon} \text{ (Radial wall shear stress)}$$

$$\tau_{z\theta} = \frac{r w_s}{w_s} \text{ (Swirl wall shear stress)} \tag{6}$$

The torque acting on the plates can be found by integrating this shear stress over the surface area:

$$T = \int_0^{2\pi} \int_{R_i}^{R_o} \tau r^2 dr d\theta = \int_0^{2\pi} \int_{R_i}^{R_o} \frac{\nu_s}{w_s} r^3 dr d\theta.$$

This expression for torque is proportional to the rotational velocity and inversely proportional to the clearance between the two plates. Torque increase due to increasing speed can be attributed to steeper gradients at the wall. Increasing clearance results in reduction of these gradients and hence the torque reduces as well.

3 2D FLUENT Overview and Modeling

Overview. To verify the model, results were obtained from the computational fluid dynamics package FLUENT that satisfies the full Navier-Stokes equations. As a result, we need additional boundary conditions at $r=R_i$ and R_o. Apart from the boundary conditions mentioned on the velocities at the wall, natural boundary conditions are specified at the inlet. The pressure condition is specified on the outlet, i.e., the pressure is atmospheric and the inlet pressure is left unspecified. Instead flow rate is specified and that allows us effective comparisons with experiments.

Physical Specifications. The computational grid was set up using "GAMBIT," the standard grid generating package used for FLUENT. The physical quantities assumed for generating the grid are as follows:

$$R_i = 0.95$$

$$R_o = 1.05$$

Grid Generation. The grid used 150 equally spaced points in the radial direction and 100 points in the axial direction. The grid points in the axial direction were placed symmetrically about midplane between the two walls using a ratio of 1.05 to separate adjacent grid points. This forms a dense mesh in the near wall region to resolve higher gradients near the wall.

Solver. The FLUENT solver used for computations was "axisymmetric with swirl." Such a solver made it possible to model a three dimensional flow (since all three components of velocity exist) using a two-dimensional geometry. The swirl velocity represents the tangential component of velocity "ν." The fluid modeled in the computations was a standard automatic transmission fluid with $\mu=0.048$ Ns/m^2, $\rho=960$ kg/m^3. The angular velocity was set at 2000 rpm. Under-relaxation parameters for pressure and momentum were set slightly below one. This stabilizes the solution procedure but on the flipside the iterations take longer to converge. The convergence criteria were set as 0.001 for residuals of the three components of velocity and continuity.

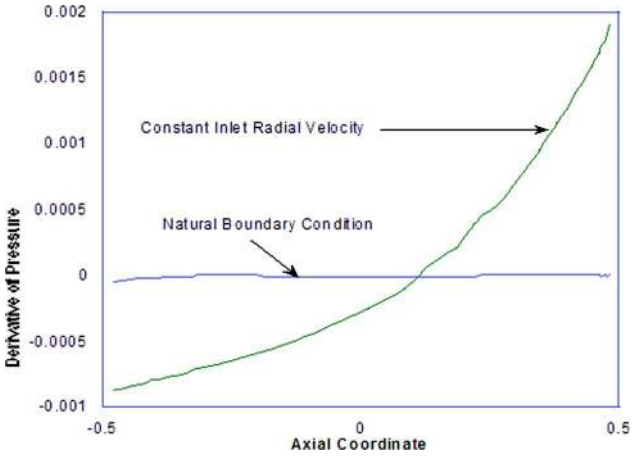

Fig. 3 Axial derivative of pressure at the inlet for different boundary conditions. The natural boundary condition shows that $\partial p/\partial z \approx 0$, in agreement with the asymptotics. Derivative of pressure is normalized with $\rho\nu_s^2/h$ and axial coordinate by h.

Specification of Boundary Conditions. The boundary condition at the outer radius was set to the "pressure outlet" condition. The gauge pressure was set to 0. Different inlet conditions were tried. Constant radial velocity profile, the mass flow inlet and the natural boundary conditions were used. The solution obtained was similar in each case except that there were some differences in the very small region near the inner radius. This was observed because FLUENT had to adjust from the given velocity profile to the actual profile obtained. Once the actual velocity profile was obtained, the results showed very good consistency between each other.

Figure 3 shows that the pressure strongly depends on z at the region near inner radius if the inlet boundary condition is given as a constant radial velocity profile. This contradicts the results obtained from the model. However, if the natural boundary conditions are used at the inlet, then $dp/dz=0$ and this is consistent with the results of the model. Once sufficiently inside the domain, i.e., at about 1 mm beyond inner radius, this anomaly is remedied in both inlet profiles and the pressure truly becomes independent of z.

It should be noted that FLUENT does not permit specifying natural boundary conditions at the inlet. The "outflow" condition specifies natural boundary conditions on the outlet. To specify natural boundary conditions at the inlet, we:

- created a preliminary grid such that its outer radius is equal to the actual grid's inner radius
- specified "outflow" boundary condition on its outlet and solved the solution
- saved the velocity profiles at its outlet and prescribed them on the inlet of the actual grid.

Solution Profiles. Presented below are some FLUENT results for the case where gauge pressure at both the inner and outer radius is zero. The profile of pressure in the radial direction is parabolic. The second term on the right hand side (RHS) of (5) has a quadratic dependence on radius and hence the nature of the curve. Therefore the dominant term in (5) is known, justifying the assumption that the scale for pressure should be inertial rather than viscous. Viscous scaling would have been more appropriate for a logarithmic pressure profile.

The second set of results, Figs. 4 and 5 are for radial and axial

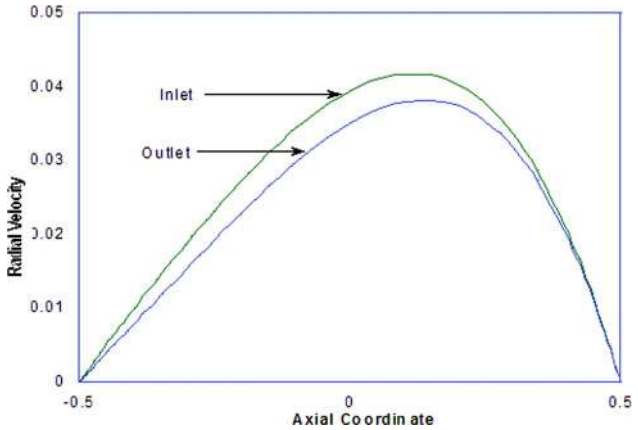

Fig. 4 Radial velocity versus axial coordinate. Radial velocity normalized with $\omega^2 R_m h^2 \rho/\mu$ and axial coordinates by h.

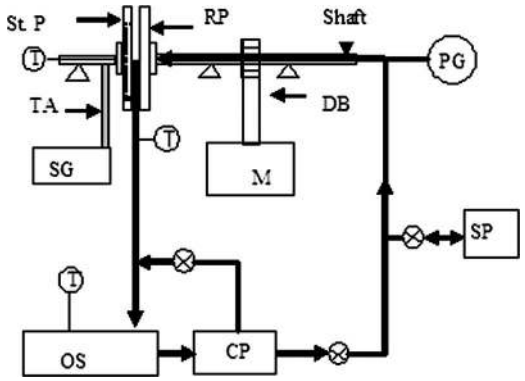

Fig. 6 Block diagram of overall system configuration. The circulation pump helps to maintain a steady oil temperature throughout. The syringe pump is used whenever a fixed flow rate of oil is to be prescribed. St. P: Stationary plate, RP: Rotating Plate, TA: Torque arm, T: Thermocouple, M: Motor, PG: Pressure gauge, SG: Strain gauge, DB: Driving belt, SP; Syringe pump, OS: Oil sump, CP: Circulation pump.

velocity profiles and their relative magnitudes. The plots are nondimensionalized with their respective scales. The tangential velocity profile obtained was linear as predicted by Eq. (3), and hence is not shown here.

The radial velocity profile obtained is slightly asymmetric with the peak shifted toward the rotating plate. The peak values decrease from inlet to the outlet as expected because of continuity. The specification of natural boundary conditions on the inlet gives a very smooth profile transition. Assuming a symmetric radial velocity can be allowed since FLUENT simulations show the asymmetry to be small at low rotation rates.

4 Experimental Apparatus

A small experimental rig was setup to test various groove patterns and verify the effects of clearance, rotation speed and groove depth. A high-speed camera visualizes the flow and the incipience of aeration. The flow periodicity that could be affected by gravity is checked visually so we can assure the veracity of simulating only a sector of the actual plate for computational efficiency.

Thermocouples monitor oil temperatures as it enters the plates and when it is ejected out from the outer radius and a heater warms the oil if needed. The temperature rise resulting from viscous dissipation between the plates is small, at most 2C, and hence viscosity can be assumed to be constant.

Figure 6 shows the overall system configuration as a block diagram. A 15 hp inverter-type motor (400–3450 rpm) drives the rotating clutch plate. Centrifugal pump supplies oil throughout the system and the pump work and friction work between the plates increases the system temperature accordingly. The oil flow rate is precisely controlled by a displacement syringe pump that compresses two 50 ml syringes at a prescribed speed. When the inlet and outlet oil temperatures reach steady state, a valve attached to the centrifugal pump is closed to stop oil supply and the accurately metered, constant displacement syringe pump starts for the torque and optical measurements. A beam type single point load cell measures the drag torque of the stationary plate.

One end of the 15 inch long moment arm is bolted to the stationary plate axis and the other end is placed on top of the load cell. This makes it possible to calculate the drag torque by multiplying the force measurement of the load cell by the moment length. A high-speed imager captures digital images through the transparent rotating plate at a rate of 4500 fps. A 500 W electrical heater installed in the oil sump allows experiments with elevated oil temperature.

Figures 7 and 8 show the photograph of the assembly and circulation system. Transparent quartz rotating disk plate allows visualization of the flow pattern. The stationary plate is made of aluminum disk. To minimize the influence of the inner circular region, the stationary plate has a 4 mm depth (very large compared to the clearances between the two plates that are 100 and 200 μm) step "d." Five different stationary plates investigate the groove effect on drag torque. Four plates are made by two different numbers of grooves (40 and 80) and 2 groove depths (200 and 400 μm) combinations and a no groove plate (flat disk) is tested for generic experiment.

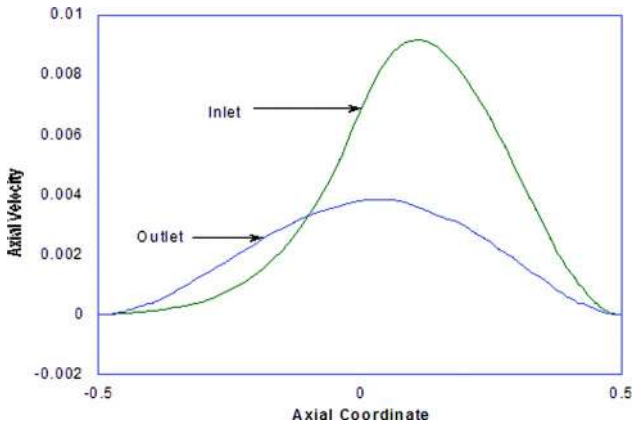

Fig. 5 Axial velocity versus axial coordinate. These are normalized by $\omega^2 h^3 \rho/\mu$ and h, respectively.

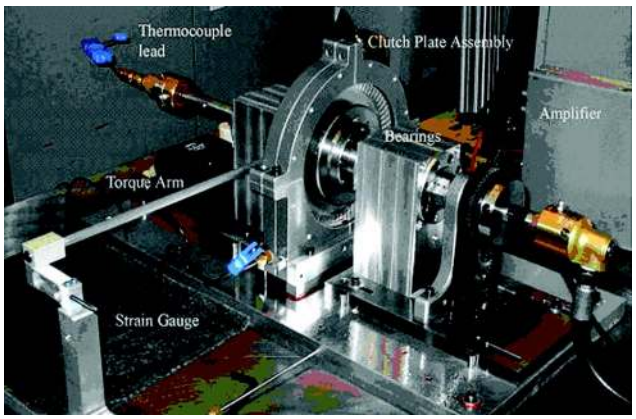

Fig. 7 Photograph of the assembly and the relevant components. The view is taken from the rotating plate side.

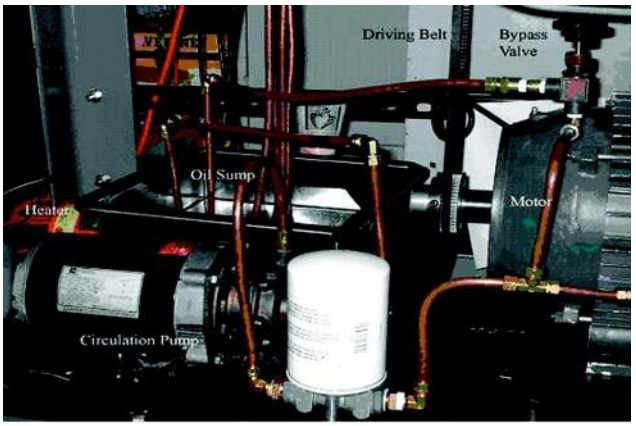

Fig. 8 Photograph of the circulation system. The oil sump is heated if required. The circulation pump maintains the oil temperature while the motor rotates one plate.

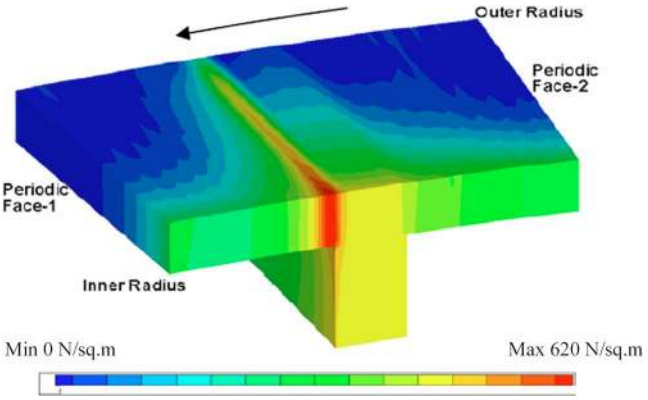

Fig. 10 Pressure contour for the 40 grooved plate and the modeled geometry. The top plate moves in anticlockwise direction. Pressure is high near the downstream notch.

The repeatability of the experiments was tested by four repeated runs on successive days. The test cases for 80 grooves, 100 micron clearance, and 100 ml/min flow rate are shown in Fig. 9. The temperature was kept nearly constant, by beginning each test with the fluid and apparatus at room temperature and keeping run times short. The standard deviation of the resulting torque is 0.03 or about 6% variation.

5 3D Single-phase Flow Modeling

Flow and Geometry Description. The experiments provide a good way to test various groove patterns. The model predicts drag torque and pressure without extensive experimentation or computation. However, the computations will help us experiment with different groove patterns without manufacturing plates. The optimization study that we will further carry out in the future can best be done using CFD. It is in this regard that the computations assume an important role in this study.

In the effort to reduce drag, we performed numerical simulations for one grooved disk with the other disk flat. The grooves were radial, as they are known to reduce drag. Eight different models were created to simulate various parameters. We varied the clearance, groove depth and the number of grooves with flow rate kept constant, as it does not significantly affect drag torque. Since the axisymmetry assumption can no longer be used, the modeling is three-dimensional. In an effort to reduce computational effort, the flow was assumed to be N-fold periodic in the θ direction. Numerical tests on varying sized domains validated this periodicity. The table below shows the specification of 8 models (2 different No. of Grooves+2 Clearance+2 Groove Depths).

No. of Grooves	Groove Depth (microns)	Clearance (microns)	Area Percentage (ungrooved:total)
40	200	100	83.4%
80	400	200	66.8%

The inner and outer radii of 7.2 and 8.13 cm, respectively, were chosen to match experiments.

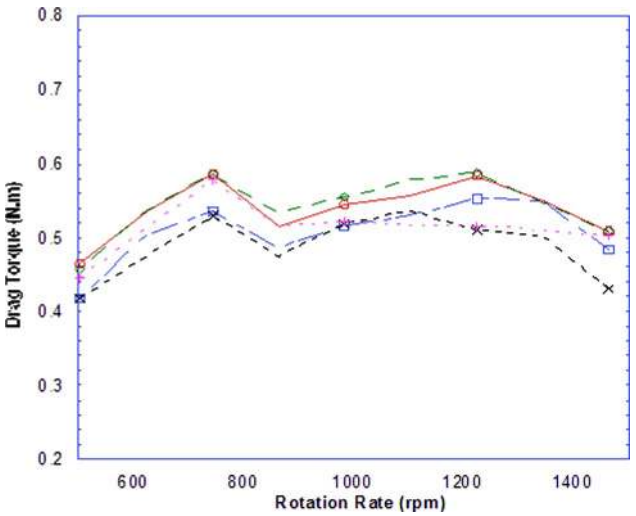

Fig. 9 Repeatability study experiments for 80 grooves, 100 micron clearance

Grid Generation and Convergence Test. GAMBIT, the standard grid package for FLUENT generated the geometry of the model. The grid had 21 by 56 by 36 node points in the radial, tangential and axial directions, respectively. The grid in the axial direction was made finer near the walls to resolve the gradients near the wall. The width of groove was 2 mm. The boundary conditions specified were natural boundary conditions at inlet, atmospheric pressure at the outlet and periodic boundary conditions on two radial faces. The flat plate rotates while the grooved plate is stationary.

To check the accuracy of our solutions, we conducted a grid convergence study as follows: The simulation for the finest grid resolution, with all three components of velocity and pressure computed were compared with results for lower grid resolutions. The error was defined as the L_2 norm of the difference between all variables of any particular resolution and the finest resolution. The tests showed the finite difference scheme to be first-order accurate.

Solution Variable Profiles and Flow Visualization. Figure 10 shows that the downstream face stagnates the oil flow and creates a high pressure region. Correspondingly, pressure at the upstream notch drops down and hence aeration can be promoted at the upstream notch near the outlet. Figures 11 and 12 show the fluid path lines in the domain. Figure 11 is the top view of the plates with the upper plate rotating. The fluid flow in the groove is predominantly in the radial direction whereas the flow in the remainder of the domain is in the tangential direction. Figure 12 shows the view from the inner radius. The axial fluid velocity is very small since the axial pressure gradient is small. The fluid in the groove shows stronger spiral motion.

Figure 13 shows the tangential component of shear stress. The tangential shear stress on the rotating wall is fairly uniform. The tangential shear stress in the groove is low compared to the face (i.e., not in groove). This is because the flow is predominantly radial. Thus grooves can be helpful in reducing the torque.

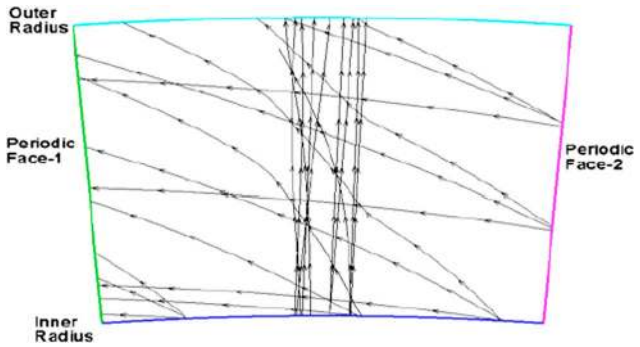

Fig. 11 Fluid path lines as viewed from the top. The fluid in the notch goes radially outward while the fluid in between the two plates moves predominantly in the tangential direction.

6 Comparison of Results

Pressure Comparisons of Model and Simulation. The pressure distribution across the disks is determined by the mass flow. The results shown in Fig. 14 always have zero gauge pressure. The gauge pressure at the inlet, however, depends on the mass flow rate. Negative or suction gauge pressure occurs at the inlet if less oil is supplied to the plates, indicating likely aeration. The comparisons shown between FLUENT and the two models are in Fig. 14. Since flow rate is the comparison parameter, we show various pressure profiles from FLUENT and the lubrication models, both exact and approximate. Comparison is within 10% and in some cases within 5%. FLUENT uses the natural boundary inlet conditions as prescribed in Sec. 3.

The model used for comparisons are

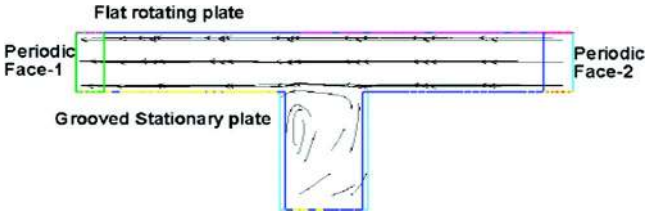

Fig. 12 Fluid path lines as seen from the inner radius. The spiraling motion of the fluid can be seen in the notch. The fluid moves in almost horizontal planes between the two disks.

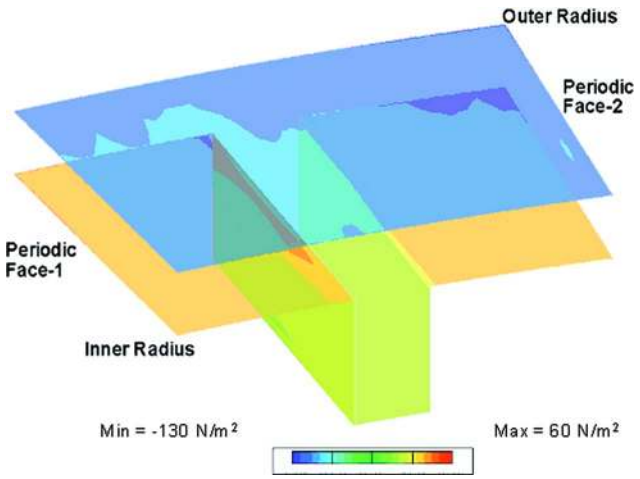

Fig. 13 Tangential component of shear stress. The rotating plate has a very large value of shear stress throughout. The grooved plate shows less tangential shear stress in the region of the notch due to predominant radial motion of fluid.

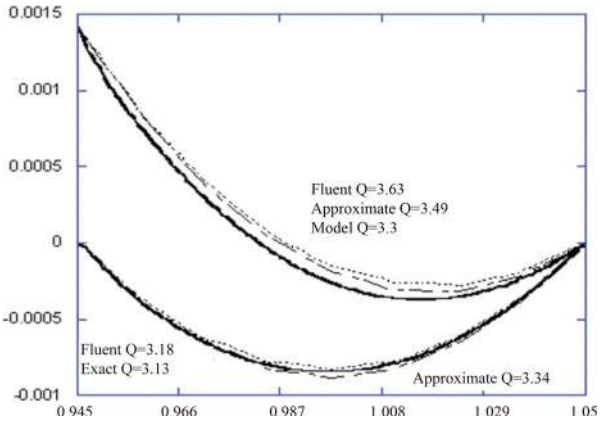

Fig. 14 Pressure comparison of FLUENT with model for three different flow rates. Pressure is normalized with ρv_s^2 and radius with R_m. The solid line is FLUENT, dotted line is the exact model and dashed line is the approximate model.

$$P - P_o = \frac{6Q}{\pi}\ln\left(\frac{R_o}{r}\right) + \frac{1}{6.25}(r^2 - R_o^2) \quad \text{Approximate solution}$$

$$P - P_o = 12\left[\frac{1}{80}(r^2 - R_o^2) - \frac{Q}{2\pi}\ln\left(\frac{r}{R_o}\right)\right] \quad \text{Exact solution}$$

The denominator in the second term in the right hand side of (5) changed form 8 to 6.25 and this is a result of changing from a factor of 0.5 to a factor of 0.565. Pressure is important because for aeration incipience.

The difference between the approximate solution and the exact solution is negligible. The simplification that the centrifugal term is independent of the z coordinate reduces the order of radial velocity profile from 4 to 2, but the solution changes are small (Fig. 15).

Shear Stress Comparison of Model and Simulations. Figure 16 shows the radial variation of shear stress as predicted by the models and FLUENT. The wall shear stress is linear in radius as predicted by (6). FLUENT predicts slightly different shear stresses for the rotating and the stationary wall, resulting in differing torques. Conservation of angular momentum for the system requires a torque imbalance between the two plates to impart angular momentum to the fluid although the difference in shear stresses is small as indicated by the stress scale in Fig. 16. Our lubrication model predicts the same shear stress values for both the stationary

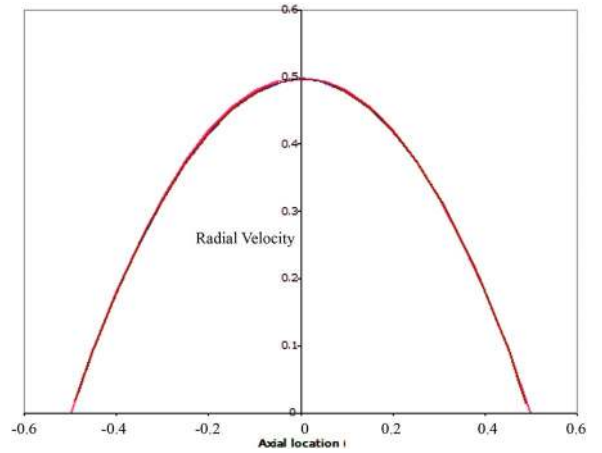

Fig. 15 Radial velocity comparison of FLUENT with models. The three curves correspond to FLUENT, exact and approximate models lie almost on top of each other.

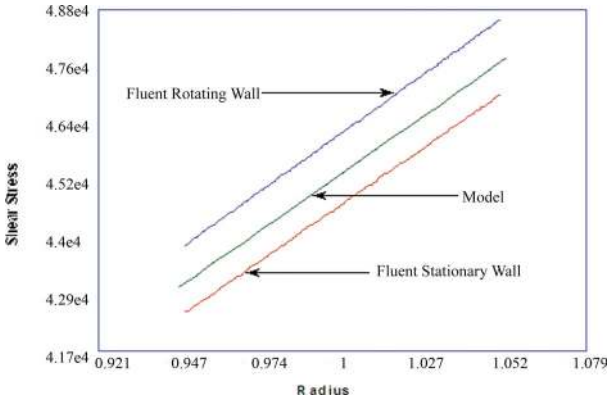

Fig. 16 Shear stress versus radius. FLUENT predicts shear stress on the stationary and rotating wall to be slightly different to give increasing angular acceleration to the fluid.

and rotating disk. The shear stress values and hence the torque given by both methods is in very close agreement.

Torque Comparisons of Model, Experiment, and Simulations. Figures 17 and 18 show the results for 2D axisymmetric flow. Figure 17 shows the drag torque versus rotational speed for the model, computations as well as experiments when the clearance is 100 microns. The drag torque increases linearly with speed. The model and simulation show results in close agreement. The experimental results are off by a factor of 1.5. Figure 18 shows the same result for the 200-micron clearance case. In this case the results are within a factor of 1.1–1.2. Correcting the clearance reduces experimental error. Hence the values match better with the 200-micron case than the 100-micron case. Also in Fig. 18 the torque values match well at 500 rpm but diverge slightly at 1500 rpm due to aeration that is not accounted for in the model and the simulation for single-phase. Aeration reduces torque as expected.

Figures 19–21 show the results of disks with grooves. Since these simulations do not include multiphase flows, the comparisons were done at low rpm (here 500 rpm). The results and trends are expected to hold true until about 1000 rpm. The approximate model is derived from the mathematical model. Since the grooves reduce the contact area of the two disks, a good engineering approximation to the problem will be to reduce the drag of the axisymmetric case by the area ratio.

This can be mathematically expressed as

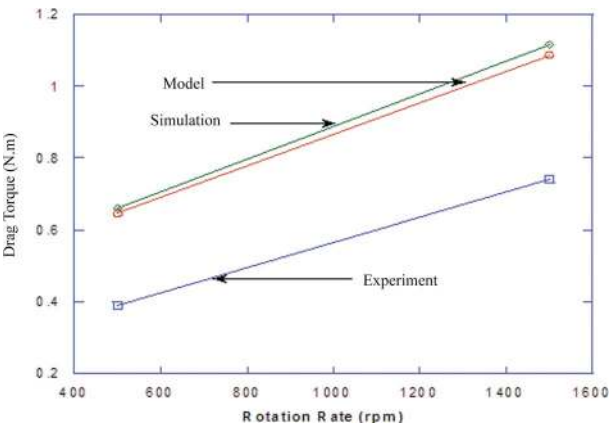

Fig. 17 Drag torque versus rotation rate at 100 microns clearance. The comparisons show that the simulation and model are in close agreement with each other.

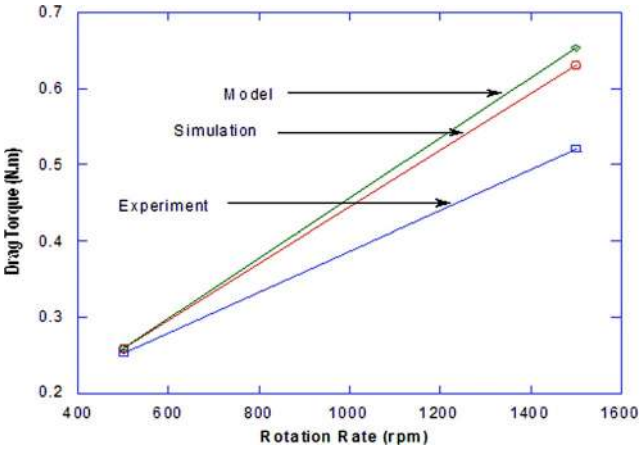

Fig. 18 Drag torque versus rotation rate at 200 microns clearance. The discrepancy between experiments and simulation is much lower than that of Fig. 17 because sensitivity of error in setting the clearance is less at higher separations.

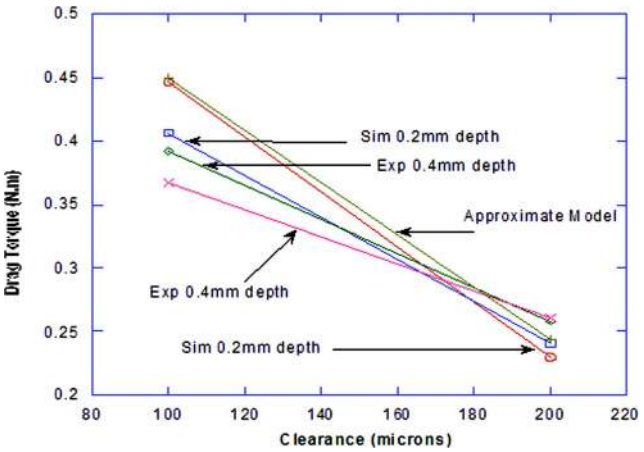

Fig. 19 Drag torque versus rotation rate for the 40 grooves per plate. The 3D single-phase simulation show excellent agreement with the experiments.

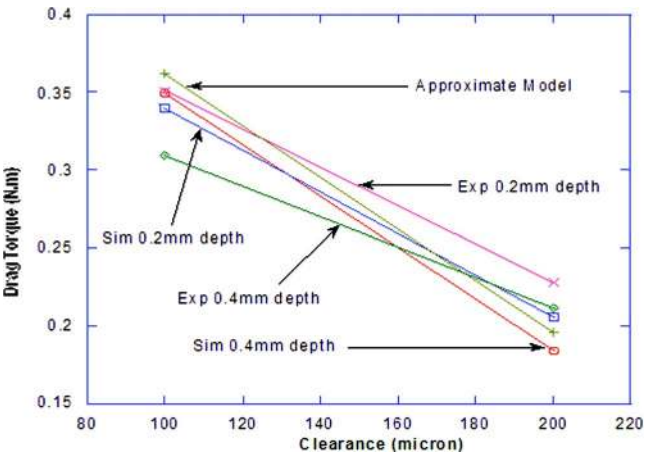

Fig. 20 Drag torque versus clearance for the 80 grooves plate. On average, the 80 groove plate shows less torque than 40 groove plate. The approximate model is valid only in the single-phase region.

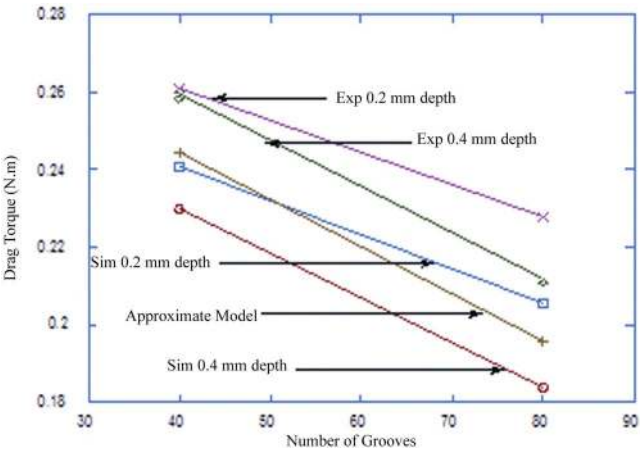

Fig. 21 Drag torque versus the number of grooves for the 200 microns clearance

$$T = \int_0^{2\pi} \int_{R_i}^{R_o} \frac{[\mathrm{vs}]}{[\mathrm{ws}]} r^3 AR dr d\theta$$

where AR is the area ratio of the grooved disk. Figure 19 shows the variation of torque with clearance for the 40 grooves per disk case. The torque drops with increasing clearance because the gradients near the wall are higher for lower clearances. The approximate model matches well with simulations. The experimental results also match within a factor of 1.5. Figure 20 shows the same result but for the 80 grooves per plate case. The torque values for experiment, simulation and approximate model match closely at both clearances. Figure 21 shows the relation between torque and the number of grooves at 200-micron clearance case. The 80 grooves plate shows significantly less torque than the 40 grooves plate. Figure 13 shows that the tangential component of shear stress in the region of groove is substantially lower than the remaining of the ungrooved plate. This reduction in shear stress is because the nature of fluid flow in the groove is entirely different from the rest of the domain. The flow in the groove is radial and so has very small gradients in the tangential direction. The 80 grooves plate has more surface area covered with grooves (since their width was kept constant at 2 mm) than the 40 grooves per plate case. This fact manifests itself into reducing torque on the 80 grooves plate. However, there is a practical constraint on increasing the number of grooves. The engagement of the clutch is its primary function and increasing the number of grooves reduces its engagement properties. Hence, there is a limitation on increasing the number or size of grooves.

7 Conclusions

The lubrication model derived in this paper closely matches the results from computations and experiments for both the shear stress and pressure distributions. The derived exact lubrication model is only slightly more involved than the approximate model representative of lubrication theory velocity. The differences between the results of these two models are insignificant. The computations show that the radial motion of the fluid in the grooves causes a significant drop in the tangential component of shear stress resulting in reduced torque. This also explains why sunburst and spiral grooves increase torque since the motion of fluid in the groove is primarily in the tangential direction. The pressure distribution suggests that the onset of aeration happens near the outer radius of the upstream notch. On comparing experiments, computations and models, clearance has the most significant effect on reducing drag torque. Increasing the number of grooves also reduces torque. However, the groove depth is not a significant parameter; at least when the groove is on the stationary disk. The expression for torque derived for the axisymmetric case can be used with fair approximation for the grooved plates by multiplying the torque in the axisymmetric case with the fraction of area which is not grooved. This method is valid only if the entire flow is single-phase.

Acknowledgment

We acknowledge the funding by the Dynax Corporation. We are grateful to a referee that pointed out that an exact solution to the radial velocity was possible. We would like to thank Miguel Verdejo for reading the manuscript and suggesting modifications.

Nomenclature

A = inlet flow area m^2
Q = volumetric flow rate between disks
Re = Reynolds Number
d = depth of the stationary plate notch m
h = axial clearance between disks m
p = pressure
r = radial coordinate
t = time
u = radial component of velocity
v = tangential component of velocity
w = axial component of velocity
z = axial coordinate
θ = tangential coordinate
μ = dynamic viscosity Ns/m^2
ρ = density kg/m^3
ω = angular velocity in rad/s
τ = shear stress
R_i = inner radius
R_m = mean radius $(R_i+R_o)/2$
R_o = outer radius
p_o = atmospheric pressure
u_s = radial component of velocity scale m/s
v_s = tangential component of velocity scale m/s
w_s = axial component of velocity scale m/s
τ_{zz} = normal component of shear stress on disks
$\tau_{z\theta}$ = tangential component of shear stress
τ_{zr} = radial component of shear stress on disks

References

[1] von Karman, Th., 1921, "Laminar and Turbulent Reibung," Z. Angew. Math. Mech., **1**, pp. 233–252.
[2] Cochran, W. G., 1934, "The Flow Due to a Rotating Disk," Proc. Cambridge Philos. Soc., **30**, pp. 365–375.
[3] Batchelor, G. K., 1951, "Note on a Class of Solutions of Navier-Stokes Equations Representing Steady Rotationally Symmetric Flow," Q. J. Mech. Appl. Math., **4**, pp. 29–41.
[4] Stewartson, K., 1953, "On the Flow Between Two Rotating Coaxial Discs," Proc. Cambridge Philos. Soc., **3**, pp. 333–341.
[5] Kitamura, A., 2000, "Asymptotic Solution for a Film Flow on a Rotating Disk," Phys. Fluids, **12**(8), pp. 2141–2144.
[6] Schade, C. W., 1971, "Effects of Transmission Fluid on Clutch Performance," SAE Paper No. 710734.
[7] Fish, R. L., 1991, "Using the SAE #2 Machine to Evaluate Wet Clutch Drag Losses," SAE Technical Paper Series No. 910803.
[8] Lloyd, F. A., "Parameters Contributing to Power Loss in Disengaged Wet Clutches," SAE Paper No. 740676.
[9] Debuchy, R., Dyment, A., and Muhe, H., 1993, "Radial Inflow Between a Rotating and a Stationary Disc," C. R. Acad. Sci., Ser. II: Mec., Phys., Chim., Sci. Terre Univers, **317**, Serie II, pp. 437–442.
[10] Gori, F., 1985, "Is Laminar Flow in a Cylindrical Container Within a Rotating Cover Batchelor or Stewartson-Type Solution?," J. Fluids Eng., **107**, pp. 436–437.
[11] Higgins, B. G., 1986, "Film Flow on a Rotating Disk," Phys. Fluids, **29**, pp. 3522–3529.
[12] Yuan, Y., Attibele, P., and Dong, Y., 2003, "CFD Simulation of the Flows Within Disengaged Wet Clutches of an Automatic Transmission," SAE Paper No. 2003-01-0320.
[13] Kitabayashi, H., Li, C. Y., and Hiraki, H., 2003, "Analysis of Various Factors Affecting Drag Torque in Multiple-Plate Wet Clutches," JSAE Technical Paper No. 20030331.